Available online at www.sciencedirect.com

ScienceDirect

Acta Materialia 61 (2013) 6765–6777

Acta MATERIALIA

www.elsevier.com/locate/actamat

Direct observation of asymmetric domain wall motion in a ferroelectric capacitor

Ja Kyung Lee [a,1], Ga Young Shin [a,1], Kyung Song [a], Woo Seok Choi [b], Yoon Ah Shin [a], Seong Yong Park [c], Jason Britson [d], Ye Cao [d], Long-Qing Chen [d], Ho Nyung Lee [b], Sang Ho Oh [a,*]

[a] Department of Materials Science and Engineering, Pohang University of Science and Technology (POSTECH), San 31, Pohang 790-784, Republic of Korea
[b] Materials Science and Technology Division, Oak Ridge National Laboratory, Oak Ridge, TN 37831, USA
[c] Analytical Science Group, Samsung Advanced Institute of Technology (SAIT), Yongin 446-712, Republic of Korea
[d] Department of Materials Science and Engineering, The Pennsylvania State University, University Park, PA 16802, USA

Received 3 June 2013; received in revised form 17 July 2013; accepted 24 July 2013
Available online 3 September 2013

Abstract

We report in situ transmission electron microscopy observations of the 180° polarization switching process of a $PbZr_{0.2}Ti_{0.8}O_3$ (PZT) capacitor. The preferential, but asymmetric, nucleation and forward growth of switched *c*-domains were observed at the PZT/electrode interfaces, arising due to the built-in electric field induced at each interface. The subsequent sideways growth of the switched domains was inhibited by the depolarization field due to the imperfect charge compensation at the counter-electrode and also at the boundaries with preexisting *a*-domains, which contributed further to the asymmetric switching behavior. It was found that the preexisting *a*-domains split into fine *a*- and *c*-domains constituting a 90° stripe domain pattern during the 180° polarization switching process, revealing that these domains also actively participated in the out-of-plane polarization switching. The real-time observations uncovered the origin of the switching asymmetry and further clarified the importance of charged domain walls and the interfaces with electrodes in the ferroelectric switching processes.

Keywords: In situ transmission electron microscopy; Ferroelectric thin film; Polarization switching; 90° Domains; Depolarization field

1. Introduction

The spontaneous polarization in ferroelectrics can be switched by applying an electric field. The polarization switching occurs through the nucleation and subsequent forward and sideways growth of the switched domains [1,2]. The reversible switching capability has been explored extensively for a wide range of applications, including transistors and memory devices. In the technically important $Pb(Zr_{1-x}Ti_x)O_3$ (PZT) thin film capacitors, switching between two bistable polarization states that are related by a 180° rotation is implemented by applying a uniform electric field across the film. Generating a uniform field requires the use of two planar electrodes on the top and bottom surfaces of PZT thin film. It has been demonstrated that the nature of the ferroelectric/electrode interfaces has significant effects on the switching characteristics of a ferroelectric capacitor [3–6]. For example, practical ferroelectric/electrode interfaces allow polarization switching to occur at much lower coercive fields (E_C) than the theoretical predictions assuming ideal interfaces [7,8]. Moreover, the electrical boundary conditions of the top and bottom electrodes are often not identical, which lead to asymmetric switching between the two polarization states [5,9,10].

* Corresponding author. Tel.: +82 (0)54 279 2144; fax: +82 (0)54 279 2399.
E-mail address: shoh@postech.ac.kr (S.H. Oh).
[1] These authors contributed equally to this work.

1359-6454/$36.00
http://dx.doi.org/10.1016/j.actamat.2013.07.051

In practical PZT thin film capacitors, domains with an unfavorably oriented polarization are frequently present, which further challenge understanding of the ferroelectric switching behavior. One notable example is the ferroelastic *a*-domain with a polarization rotated 90° from that of the active ferroelectric *c*-domains. It has been reported that *a*-domain walls are immobile [11–13] and act as nucleation centers for the switched *c*-domains [13,14]. Although the question whether these *a*-domains retain their in-plane polarization or undergo internal switching during the 180° switching of the out-of-plane polarization has been discussed recently, it has not been properly addressed due to the lack of convincing experimental observations.

Therefore, understanding the detailed influence of the internal boundaries in polarization switching, such as the electrode interfaces and the boundaries with unfavorably oriented domains, is critical for future engineering of novel ferroelectric devices. In this paper, in situ transmission electron microscopy (TEM) observations of the dynamic motion of domain walls during the 180° polarization switching of a ferroelectric PZT thin film capacitor with planar Ni (top) and $SrRuO_3$ (SRO; bottom) electrodes are presented. The asymmetric electrode configuration was employed in order to distinguish the characteristic roles of the metal and oxide electrodes in the nucleation and growth of the switched domains. A 110 nm thick PZT film was chosen for this study because at this thickness the film contains both the ferroelastic *a*-domains and dislocations that form to relax the misfit strain [15,16]. As these defects are ubiquitous in this type of ferroelectric capacitor, their influences on the domain wall motion have critical effects on the remnant polarization, switching speed and numerous reliability issues in ferroelectric thin film capacitors [11,17,18].

2. Experimental procedures

2.1. Preparation of PZT capacitor with planar metallic electrodes

A 110 nm thick epitaxial $Pb(Zr_{0.2}Ti_{0.8})O_3$ film was grown epitaxially on a 20 nm thick SRO buffered Nb-doped $SrTiO_3$ (0 0 1) (Nb:STO) substrate by pulsed laser deposition [16]. The use of the conductive Nb:STO (0 0 1) substrate was considered to make it easy for the SRO bottom electrode to be connected to an electrically grounded Cu support grid. The Ni and Ti bilayer thin films were deposited on top of the PZT film by e-beam evaporation to a total thickness of ~350 nm. While the Ni thin film served as the top electrode constituting a metal–ferroelectric–metal (MFM) structure, the Ti thin film served as a contact pad to a Pt–Ir surface probe (see Fig. 1a). The bilayer electrode design minimizes the mechanical strain imposed on the PZT film upon contact of the surface probe. This configuration also allows an electric field to be applied homogeneously across the whole active area of the PZT film under the Ni electrode.

It is emphasized that the double planar electrode configuration adopted in this study offers unprecedented advantages over the configurations in previous studies using a tip-based point electrode in piezoresponse force microscopy [19,20] and recent in situ TEM experiments [17,18,21,22]. First, the dynamic motion of the switched *c*-domains can be examined under a uniform electric field over a large active area ($0.1 \times 1.2\ \mu m^2$ in lateral size). Second, the additional piezoelectric and flexoelectric coupling effects on the spontaneous polarization that may arise from the forced contact of the probe against the film surface can be avoided [23,24]. Third, but most importantly, the use of top and bottom electrodes and the current flowing between these two electrodes described using the *I–V* characteristics of ideal back-to-back Schottky diodes (shown in Fig. 1a and b and discussed in Section 3.1) ensure that the electrical boundary conditions closely resemble those in an actual ferroelectric capacitor [1].

2.2. TEM sample preparation and in situ TEM

A cross-sectional specimen of the MFM capacitor for in situ TEM was prepared by utilizing a focused ion beam (FIB, Helios NanoLab™, FEI) lift-off technique. The Nb:STO substrate of the cross-sectional TEM lamellar specimen was attached to one of the sample mounting posts of the Cu support grid by depositing a layer of conductive Pt using the FIB. The lamellar specimen was isolated into several parts by cutting vertical trenches to suppress possible leakage current of the MFM capacitor. At the final stage of milling, a low energy Ga^+ ion beam at 1 kV was used. The prepared TEM specimen was mounted on a Au wire using Ag epoxy and then the sample assembly was fixed to the piezo-stage of a STM-TEM holder (Nanofactory™). While the SRO bottom electrode of the MFM capacitor was electrically grounded through the conductive Nb:STO and the Cu support grid, the Ti/Ni top electrode was positioned to make contact with a Pt–Ir surface probe installed in the TEM holder for applying a bias. A field-emission TEM operated at 200 kV (JEM-2100F, JEOL) was used in this experiment. Real-time movies were acquired with a CCD camera (ORIUS 200D, Gatan) at 25 frames s^{-1}.

2.3. Diffraction contrast TEM imaging of switched c-domains

Conventional diffraction contrast TEM in bright-field (BF) mode was used to distinguish the *c*-domains with opposite polarization. In the case of a (0 0 1)-oriented tetragonal PZT film, the ferroelectric domains with antiparallel polarization orientations, i.e. $\mathbf{P}_{[001]}$ and $\mathbf{P}_{[00\bar{1}]}$, could be distinguished easily under the diffraction contrast owing to their different diffraction intensities. In general, for a centrosymmetric crystal structure, Friedel's law dictates that the intensities of two reflections with the reciprocal lattice vectors of $\mathbf{g}$ and $-\mathbf{g}$, $I_{\mathbf{g}}$ and $I_{-\mathbf{g}}$, respectively, are the

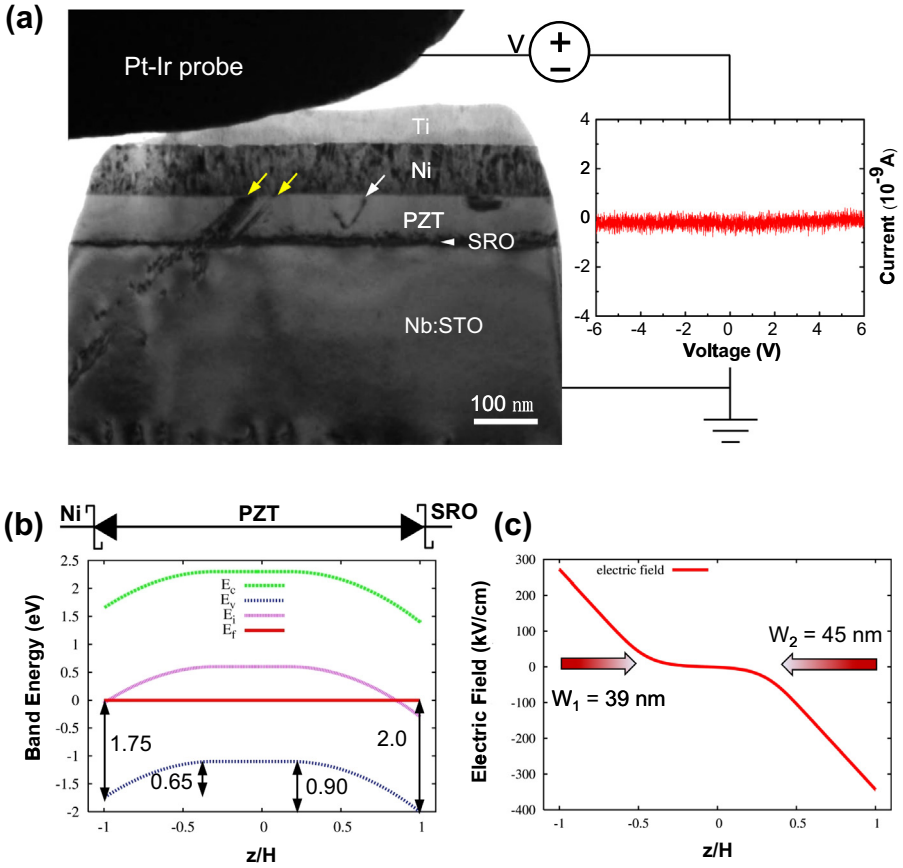

Fig. 1. Microstructure and electrical properties of a Ni/PZT/SRO MFM capacitor prepared for in situ polarization switching in TEM. (a) Cross-sectional TEM specimen prepared using the FIB lift-off method. A separate Pt–Ir surface probe was used to apply a DC bias to the Ni top electrode, while the conductive Nb:STO substrate attached to an electrically grounded Cu grid. Ferroelastic *a*-domains and a threading dislocation are indicated by the yellow and white arrows, respectively. The current in the *I–V* curve measured during a cycle of DC switching remained constant at ± 0.5 nA. (b) Energy band diagram calculated for the Ni/PZT/SRO contact system assuming thermal equilibrium. (c) Built-in electric fields calculated for the Ni/PZT/SRO contact system. The red graded arrows indicate the relative strength and direction of the built-in fields within the charge depletion zones.

same. However, in a relatively thick crystal with no center of symmetry, which is the case for our PZT sample, the failure of Friedel's law, i.e. $I_{\mathbf{g}} \neq I_{-\mathbf{g}}$, is known to take place due to the strong dynamical diffraction effect [25,26]. Indeed, the two polar domains with antiparallel polarization orientations are distinguished with different diffraction intensities under the two-beam condition, either at $\mathbf{g} = 002$ or $00\bar{2}$. The resolution of the diffraction contrast TEM is limited mainly by the size of the objective lens aperture, which corresponds to ~0.38 nm in our experiment. The real-time TEM movies were analyzed to measure the area fraction of switched domains and their moving rate as a function of applied field. The error bars in the measurements were calculated by taking account of the limited resolution of diffraction contrast imaging and the finite pixel size of recorded images, which correspond to 3.1 nm.

2.4. Phase field modeling

Phase field modeling was carried out in order to rationalize the in situ observations. In phase field simulations the temporal evolution of the ferroelectric polarization is modeled by numerically minimizing the total free energy, F, of the system with respect to a set of phase parameters, P, by iteratively solving the time-dependent Ginzburg–Landau equation [27–30]:

$$\frac{\partial P_i(r,t)}{\partial t} = -L\frac{\delta F}{\delta P_i(r,t)}, \quad (i = 1,2,3) \tag{1}$$

Ferroelectric systems can be represented by choosing the spontaneous polarization vector, $P = (P_1, P_2, P_3)$, as the order parameter to describe the ferroelectric transition and domain structures. The total free energy F of a PZT single crystal is expressed as [28].

$$F = \int_V [f_{\text{lan}}(P_i) + f_{\text{grad}}(P_{i,j}) + f_{\text{elas}}(P_i, \varepsilon_{ij}) + f_{\text{elec}}(P_i, E_i)]dV \tag{2}$$

where V is the system volume and $f_{\text{lan}}(P_i)$, $f_{\text{grad}}(P_{i,j})$, $f_{\text{elas}}(P_i, \varepsilon_{ij})$ and $f_{\text{elec}}(P_i, E_i)$ are the Landau–Devonshire energy density, the gradient energy density, the elastic energy density and the electrostatic energy density, respectively.

The strain components, ε_{ij}, are obtained by satisfying the mechanical equilibrium condition $\sigma_{ij,j} = 0$, where σ_{ij} are stress components. The electric field component, E_i, of the thin film were found by solving Poisson's equation, considering charges only due to gradients in the polarization field:

$$\begin{aligned} \varepsilon_0 \varepsilon_r \varphi_{,ii} &= P_{i,i} \\ E_i &= -\varphi_{,i} \end{aligned} \tag{3}$$

in which ε_0, ε_r and φ are the vacuum permittivity, dielectric constant and electric potential, respectively. Detailed expression of energy densities in Eq. (2) can be found in the literature [28–30].

The temporal evolution of the distribution of polarization in the system was obtained by iteratively solving Eq. (1) using the semi-implicit Fourier spectral method. The appropriate material constants of $Pb(Zr_{0.2}Ti_{0.8})O_3$ for the Landau polynomial, electrostrictive effect, electric properties and elastic properties required for expressing the system energy in Eq. (2) were collected from the literature [28,29,31–36].

3. Results

3.1. Asymmetric nucleation and forward growth of switched c-domains

The prepared TEM sample of the MFM capacitor is shown in Fig. 1a with a sketch of the electric measurement circuit and a typical *I–V* curve measured during one cycle of switching. The PZT film contained segments of a threading dislocation and *a*-domains, as indicated by the white and yellow arrows in Fig. 1a, respectively. Fig. 1b and c shows the energy band diagram and the built-in field of the Ni/PZT/SRO MFM structure, respectively, which were calculated with the assumption that the system is at thermal equilibrium. The work functions used for Ni and SRO were 5.15 eV and 4.9 eV, respectively. The PZT film was assumed to be a *p*-type wide band gap semiconductor with a hole concentration of $\sim 5 \times 10^{19}$ cm^{-3}, a band gap energy of 3.4 eV and an electron affinity of 3.5 eV [18]. The Schottky barrier heights formed at the Ni/PZT and PZT/SRO interfaces were 1.75 eV and 2.0 eV, respectively (Fig. 1b). The maximum built-in fields (E_m) and charge depletion zones (W) were calculated to be $E_{m1} = 337$ kV cm^{-1} and $W_1 = 39$ nm at the Ni/PZT interface and $E_{m2} = -397$ kV cm^{-1} and $W_2 = 45$ nm at the PZT/SRO, respectively (Fig. 1c). Throughout the DC voltage sweep cycles, the leakage current remained constant at ± 0.5 nA up to ± 6 V (Fig. 1a). The measured *I–V* characteristic appears to be similar to that one would expect from an ideal back-to-back Schottky diode (see the schematic representation in Fig. 1b) [37,38]. However, since the measured currents are limited by the instrument resolution, it is not possible to evaluate the exact transport mechanism of our PZT capacitor.

The direct in situ TEM observations of the polarization switching processes demonstrate that the ferroelectric/electrode interfaces are the preferential nucleation sites for 180° switched *c*-domains. Interestingly, the domain nucleation was asymmetric and occurred only at the positively biased PZT/electrode interface (Figs. 2 and 3; also see Supplementary movies 1, 2, and 3). Upon nucleation, the switched domains propagated forward along the field direction. The asymmetric nucleation can be explained by the presence of a built-in electric field at each electrode [3,5,18]. In the Ni/PZT/SRO MFM contact system, these fields are antiparallel to each other and point to the interior of the PZT film with their maximum values at the interfaces (Fig. 1c). The nucleation of the switched domains occurred preferentially at the PZT/electrode interface where the built-in field was oriented in the same direction as the applied field. The result strongly suggests that the built-in field adds positively to the applied field, which decreases the nucleation barrier [3,5,18]. During the forward growth, the switched *c*-domains maintained a characteristic triangular tapering in order to reduce the density of the positive bound charges at the leading edge of the domain wall with a head-to-head polarization [39,40]. The contribution of built-in field to the nucleation and forward growth of the switched domains was verified through phase field modeling and is discussed in Section 4.1.

3.2. Asymmetric sideways growth of switched c-domains

As a result of the asymmetric nucleation behavior favoring one specific electrode in the MFM capacitor, the opposite electrode served as the counter-electrode receiving the switched domains. Once the apex of a switched domain reached the counter-electrode through the forward growth, the domain continued growing along the interface with sideways movement of the domain walls, which increased the lateral extent of the switched domain. The sideways growth was critically affected by this counter-electrode, which in turn influenced the evolution of the domain pattern and switching kinetics. When a positive bias was applied to the Ni top electrode (generating a field for negative switching to the $\mathbf{P}_{[00\bar{1}]}$ state), the forward growth of a few domains dominated all others (e.g. domains labeled as A and B in Fig. 2a; see Supplementary movie 1). As soon as these domains reached the SRO electrode, they spread laterally through fast sideways growth and merged with neighboring domains into a single domain with maintaining vertical, i.e. charge neutral, domain walls. The fast sideways growth of these domains dominated the overall switching of the entire PZT film. In other words, the rate-limiting step was the forward growth of the switched domains after nucleation. In contrast, when the Ni electrode was negatively biased (generating a field for positive switching to the $\mathbf{P}_{[001]}$ state), most switched domains nucleated at the PZT/SRO interface grew forward to reach the Ni electrode at a similar rate. During the forward growth, the switched domains merged with neighboring domains,

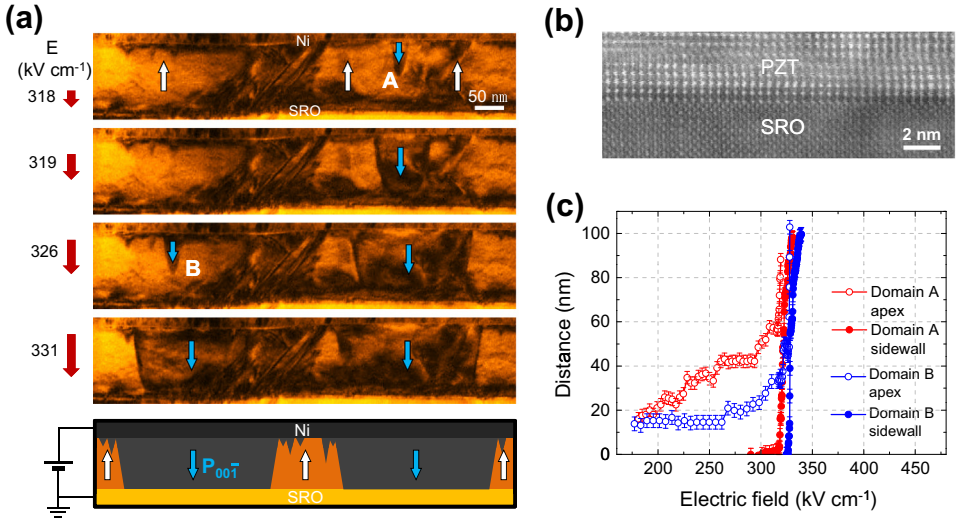

Fig. 2. Asymmetric nucleation followed by forward growth-limited switching. (a) A series of TEM images and a schematic drawing that illustrates the nucleation at the interface with positively biased Ni electrode followed by forward growth-limited switching. The forward growth rate of domains labeled as A and B was higher than all other domains nucleated at the Ni/PZT interface. The original grayscale contrast was converted to a false color scale in order to enhance the contrast. (b) A high resolution scanning TEM image of the PZT/SRO interface. The epitaxial interface is atomically smooth without any interface layers. The interface contained misfit dislocations with an average spacing of 55 ± 7 nm (refer to Fig. 5). (c) Distance of the domain walls traveled along the forward (open circles) and sideway (solid circles) directions for domain A and B plotted as a function of the electric field.

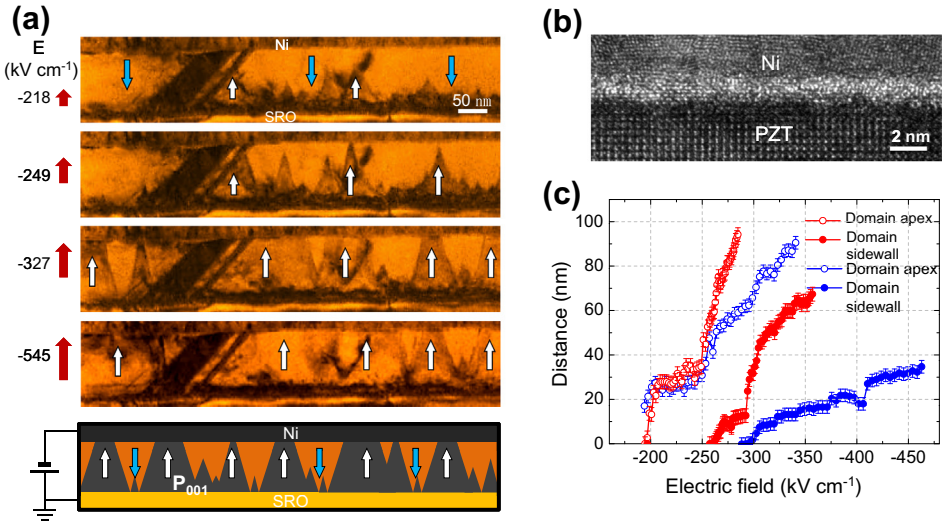

Fig. 3. Asymmetric nucleation followed by sideways growth-limited switching. (a) A series of TEM images and a schematic drawing that illustrate the domain nucleation at the interface with positively biased SRO electrode followed by sideways growth-limited switching. The original grayscale contrast was converted to a false color scale in order to enhance the contrast. (b) A high resolution TEM image of the PZT/Ni interface. The interface is interrupted by a ~1.5 nm thick intermediate layer. (c) Distance of the domain walls traveled along the forward (open circles) and sideway (solid circles) directions plotted as a function of the electric field. The sideways growth of the domains became sluggish after reaching the Ni top electrode and the average velocity remained even lower than that of the forward growth.

which produced a zigzag-shaped domain pattern (Fig. 3a; Supplementary movie 2). After reaching the Ni top electrode, however, the sideways growth of the domains stagnated (Fig. 3c). Moreover, some domain walls became pinned at the Ni electrode interface, which resulted in unswitched domains adjacent to the electrode. Thus, the rate-limiting step during the positive switching to the $\mathbf{P}_{[001]}$ state was the sideways domain growth.

3.3. Asymmetry of P-E hysteresis loop: Ferroelectric imprint

The switching asymmetry was quantitatively characterized in terms of the shift of the *P–E* hysteresis loop. The areal density of the switched domains was measured on the corresponding TEM images at various electric fields and their normalized values are plotted as a function of electric field in Fig. 4. The measurement assumed that the

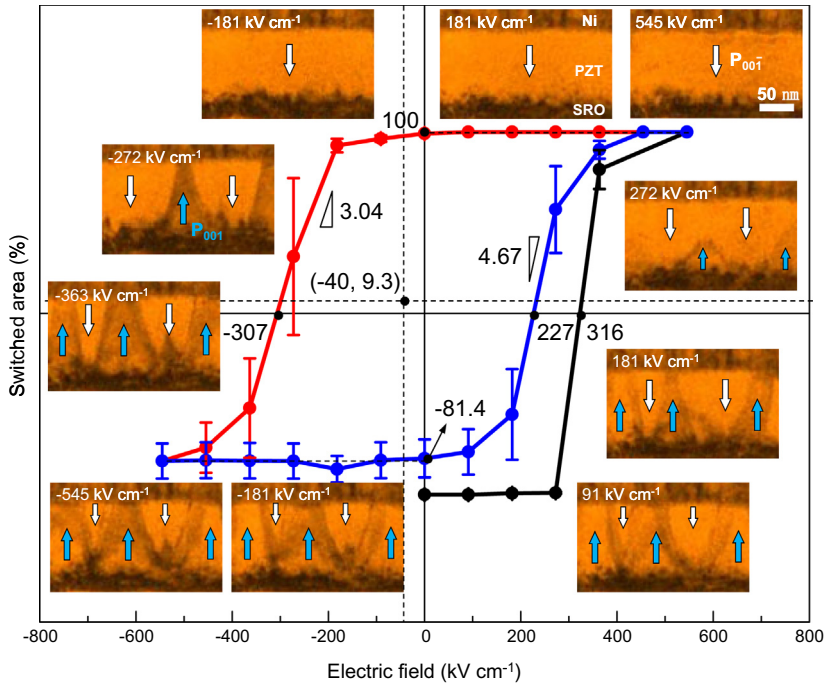

Fig. 4. Asymmetry of the *P–E* hysteresis loop. The ferroelectric hysteresis loop and corresponding footage of the TEM images recorded at various stages of polarization switching (red line for positive and blue line for negative switching) after poling (black line) to the $\mathbf{P}_{[00\bar{1}]}$ polarization. The hysteresis loop was drawn by measuring the fraction of switched area on the TEM images at various electric fields assuming that the domain widths were constant along the electron beam direction. The coercive field offset, $\Delta E_C \equiv (E_{C,N} - |E_{C,P}|)/2$, was measured to be ~40 kV cm^{-1}, where $E_{C,N}$ ~227 kV cm^{-1} and $E_{C,P}$ ~−307 kV cm^{-1} were the coercive fields for the negative and positive switching branches, respectively. A vertical shift (9.3%) toward the positive polarization axis is noted, which is due to the incomplete switching of the domains near the Ni electrode. The slope of the hysteresis curve was measured using a linear fitting of the polarization change with the electric field around E_C, which was much steeper for the negative switching to the $\mathbf{P}_{[00\bar{1}]}$ polarization than that of the positive switching to the $\mathbf{P}_{[001]}$.

domain width along the electron beam direction is the same as the TEM foil thickness for all switched domains. The *P–E* hysteresis loop exhibited a negative shift along the field axis, which is described as a ferroelectric imprint. Quantifying this shift as an offset of the coercive fields, $\Delta E_C \equiv (E_{C,N} - |E_{C,P}|)/2$ was measured to be ~40 kV cm^{-1}, where $E_{C,N}$ ~227 kV cm^{-1} and $E_{C,P}$ ~ −307 kV cm^{-1} are the coercive fields for the negative and positive switching branches, respectively. The imprint is regarded as a measure of the macroscopic built-in potential offset (ΔV_{bi}) across a ferroelectric film [9]. Considering the proposed energy band diagram of Ni/PZT/SRO MFM system, the ΔV_{bi} introduced by the work function difference is ~0.25 V. This potential offset creates a $2 \times 0.25\ \text{V} = 0.5\ \text{V}$ difference in the applied potential to switch the film (corresponding to ~45 kV cm^{-1}), which agrees well with the measured ΔE_C of ~40 kV cm^{-1}. In addition to the horizontal shift, the hysteresis loop also exhibited a vertical shift (9.3%) toward the positive polarization axis, due to the incomplete switching of the domains near the Ni electrode.

3.4. Influence of dislocations and a-domains on 180° switching of c-domains

Once the domain walls were set in a stable motion driven by a uniform electric field, the disturbance of their motions due to dislocations was negligible. When the moving front of the switched domain wall encountered a threading dislocation, its velocity was not altered with the passage (Figs. 2 and 3; Supplementary movies 1 and 2). It was also observed that the sideways growth of the *c*-domains was not delayed after impinging on the PZT/SRO interface and that unswitched regions did not remain. Note that in the 110 nm thick PZT film used in this study, misfit dislocations exist at the PZT/SRO interface along the ⟨100⟩ direction with an average spacing of ~55 ± 7 nm (Fig. 5). This indicates that the elastic or electrostatic interactions between the dislocations and (charged) *c*-domain walls were relatively weak in the 110 nm thick PZT film [41].

Unlike the ferroelectric *c*-domain walls that are mobile under electric fields, the ferroelastic *a*-domain walls remained fixed in their positions during the switching cycles. The TEM characterizations verified that these domain walls were interlocked with the misfit dislocations at the PZT/SRO interface [12,42] (Fig. 5). Previous studies have reported that the pinned *a*-domains were immobile and promoted the nucleation of the 180° switched domains at the electrode interface intersection [12,14]. In the PZT capacitor in this study, however, the nucleation was governed primarily by the interface stimulated process described above and the *a*-domain walls played only a secondary role.

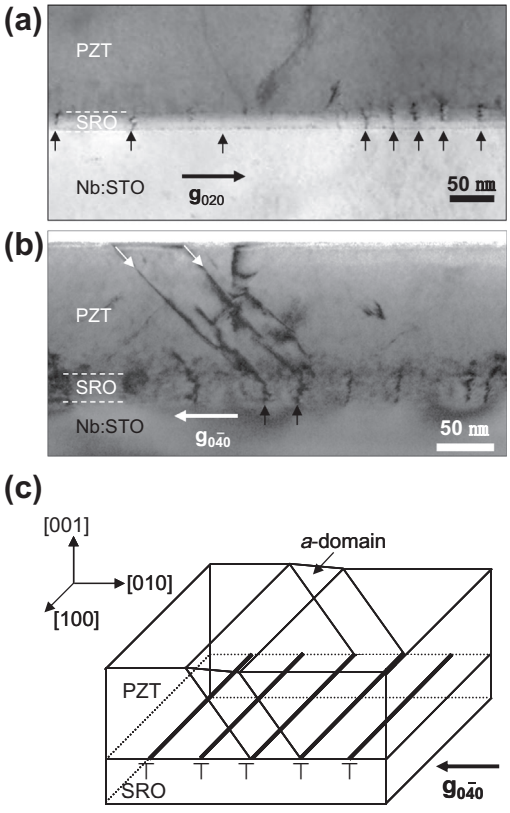

Fig. 5. Pinning of ferroelastic *a*-domain walls by misfit dislocations. (a) TEM BF image showing an array of misfit dislocations lying at the PZT/SRO interface along the [100] direction. The misfit dislocations are marked by black arrows. The TEM images were recorded at $\mathbf{g} = 020$ two-beam diffraction condition. Another pair of misfit dislocations lying along the [010] direction are invisible at this diffraction condition. (b) TEM BF image showing ferroelastic *a*-domains and an array of misfit dislocations at the PZT/SRO interface. The *a*-domains (white arrows) were pinned by misfit dislocations (black arrows) at the interface. The TEM images were recorded at $\mathbf{g} = 0\bar{4}0$ two-beam diffraction condition. (c) Schematic drawing illustrating the pinning of *a*-domains by misfit dislocations at the PZT/SRO interface.

When a certain polarization configuration was reached with the neighboring *c*-domains during the 180° polarization switching, the *a*-domains resisted the sideways growth of the *c*-domain. For example, note the sideways growth rate of the two *c*-domains A and B in Fig. 2a. Although domain B arrived at the PZT/SRO interface after domain A, it advanced quickly toward the obtuse corner of the *a*-domain wall/SRO interface whereas the sideways growth of domain A toward the acute corner was sluggish (Supplementary movie 4). Fig. 6a presents a series of TEM images that trace the sideways motion of the *c*-domain wall and the plot in Fig. 6b compares the time required for switching each corner volume. The average velocity of a switched *c*-domain wall moving to the acute corner was ~4 nm s^{-1} at ~545 kV cm^{-1}, which is almost two orders of magnitude lower than that moving toward the obtuse corner (~336 nm s^{-1} at ~328 kV cm^{-1}). The sideways movement of the *c*-domain wall toward the acute corner side required a higher electric field and a longer time span (moving from images 1 to 3 requires 8.7 s at ~545 kV cm^{-1}). In the narrow spacing of the two *a*-domains, the switching process was considerably hindered – moving from images 3 to 5 requires 20 s at ~545 kV cm^{-1} (Fig. 6a and b).

During the 180° switching of the *c*-domains, the *a*/*c*-domain boundaries become charged if the polarization of the *a*-domains remained unswitched, which would significantly affect the sideways growth rate of the *c*-domains. In the PZT film in this study, the *a*-domains established stable charge-neutral boundaries with two adjoining *c*-domains with $\mathbf{P}_{[001]}$ in a ↑/←/↑ head-to-tail configuration (refer to polarization configuration 1 in Fig. 7) [20,39]. After the 180° switching of the *c*-domain at the obtuse

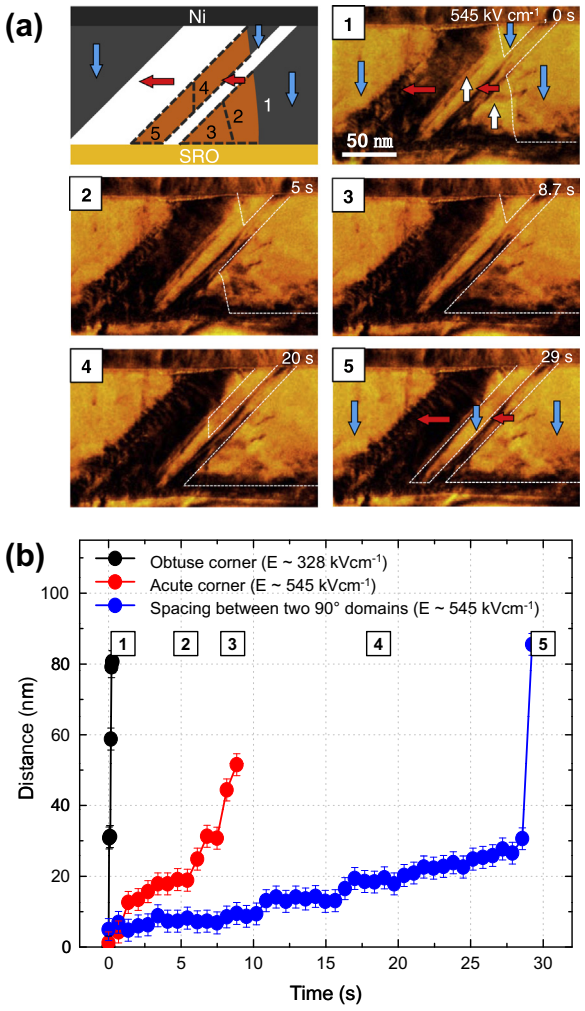

Fig. 6. Influence of the *a*-domain walls on 180° switching: delayed sideways growth. (a) A series of TEM images tracing the *c*-domain wall motion delayed in the sideways growth toward the acute wall-SRO interface corner of an *a*-domain and the spacing between two *a*-domains. The TEM images were captured from a real-time movie (Supplementary movie 4) recorded at a constant electric field (~545 kV cm^{-1}). White dotted lines were overlaid on each image to mark the location of the moving front. The original grayscale contrast was converted to a false color scale in order to enhance the contrast. (b) Plot of the distance traveled by the *c*-domain walls in the sideways growth as a function of the switching time at the constant electric fields. The data from three different geometries associated with the *a*-domains are plotted with different colors.

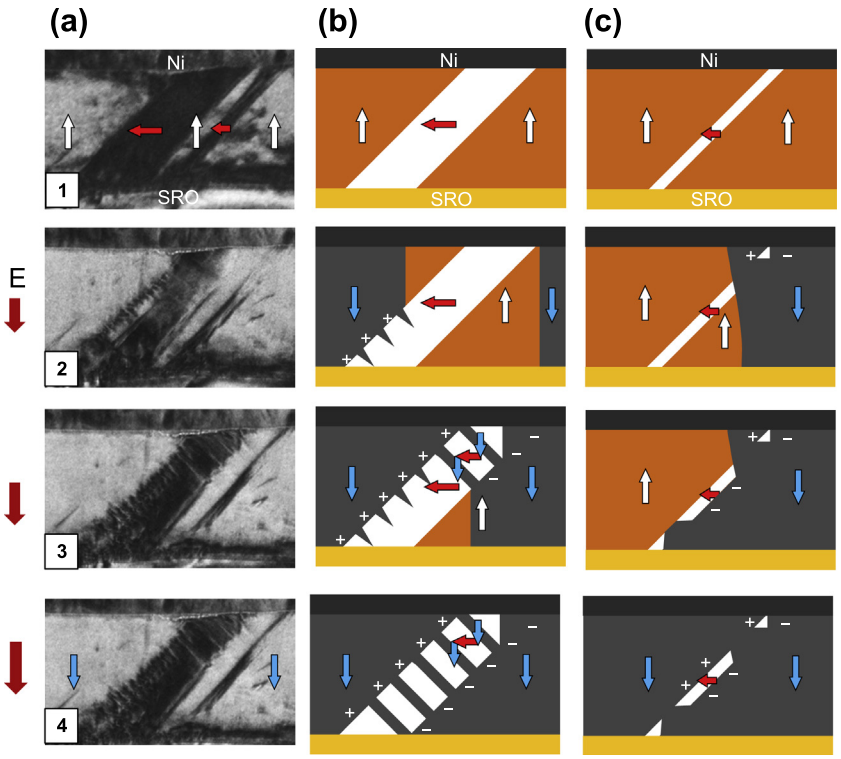

Fig. 7. Splitting of *a*-domains into 90° stripe domains: TEM observations and a model. (a) TEM images captured from a real-time movie (Supplementary movie 5) showing the splitting of the initial *a*-domains into 90° stripe domains during the 180° switching. (b, c) Corresponding schematics illustrating the formation of the 90° stripe domains within *a*-domains with different domain widths. The *a*-domains in the PZT film initially attained charge neutral boundaries with the adjoining *c*-domains with $\mathbf{P}_{[001]}$ polarization in a ↑/←/↑ head-to-tail configuration (image 1). Under an applied electric field, the 180° polarization switching usually initiated from one side of the *a*-domain first, creating a charged domain wall, e.g. the positively charged boundary at the obtuse angle corner in (b) and the negatively charged one at the acute corner in (c). When the switched *c*-domain grew along the *a*/*c*-domain boundary via sideways growth, it penetrated the *a*-domain along the boundary normal in a triangular spike in order to reduce the polarization bound charges (image 2). Switching along the opposite side of the *a*-domain resulted in the build-up of polarization charges with the opposite sign at the domain wall, which accelerated the intergrowth of the switched *c*-domain into the *a*-domain and resulted in the formation of the 90° stripe domains (image 3). The growth of 90° stripe domains with maintaining the stable head-to-tail configuration can reduce the depolarization field (image 4). For a narrower *a*-domain in (c), the depolarization field operating across the domain was significantly stronger, so that a larger portion of the *a*-domain was switched by the growing *c*-domain.

corner of the *a*-domain wall/SRO interface, however, the charge neutral *a*/*c*-domain boundary is converted to a positively charged wall with the ↓/← head-to-head configuration (configuration 2 in Fig. 7). Likewise, the 180° polarization reversal of the acute corner results in the buildup of negative polarization charges at the *a*/*c*-domain boundary due to the ←/↓ tail-to-tail polarization configuration (configuration 3 in Fig. 7). Consequently, the 180° polarization reversal of both sides of the *a*-domain converted the charge-neutral boundaries to charged boundaries with opposite polarities, which introduced a strong depolarization field across the *a*-domain. As a result of this internal field, the sideways growth of the 180° switched domain was delayed when it approached the acute corner of the *a*-domain; thus, it requires a higher electric field for the switched domains to grow toward the *a*-domain.

A flexoelectric effect due to the inhomogeneous strain fields across the *a*-domain may be responsible for the observed asymmetric sideways growth kinetics of the *c*-domains [43]. However, the strain analysis of the high angle annular dark-field images demonstrated that the 110 nm thick PZT film was almost fully relaxed without the specific strain fields associated with the *a*-domains, excluding the possibility of flexoelectric coupling effect (data not shown).

3.5. Switching of *a*-domains via 90° stripe domain formation

The charged *a*/*c*-domain boundaries created by the 180° switching of the *c*-domains are thermodynamically unstable. It was observed that the *a*-domain situated at this polarization configuration transformed into a striped domain comprised of fine *a*- and *c*-domains (hereafter referred to as 90° stripe domains) in order to reduce the density of the polarization charge and thus the depolarization field (Supplementary movie 5). A series of TEM images in Fig. 7a shows the evolution of the 90° stripe domains within the existing *a*-domain during the 180° switching. The corresponding schematics are illustrated in Fig. 7b and c for two *a*-domains with different domain widths. As the *c*-domain wall moved along the *a*/*c*-domain boundary via sideways movement (Fig. 7, second row), it began to penetrate the *a*-domain along the boundary normal in a triangular spike shape in order to reduce the density of the (positive) polarization charge at the domain

boundary [20]. Once the delayed sideways growth began at the opposite side of the *a*-domain, the depolarization field operating across the *a*-domain increased further as both domain boundaries became charged with opposite signs (Fig. 7, third row). This accelerated the intergrowth of the switched *c*-domain into the *a*-domain, resulting in the formation of the 90° stripe domains within the initial *a*-domain. Because the polarization in the 90° stripe domains attains a stable head-to-tail configuration through this transformation, the depolarization field can be reduced significantly. For narrower *a*-domains, the depolarization field operating across the domain is much stronger, so that a larger portion of the *a*-domain is switched by the growing *c*-domain (Fig. 7c).

4. Discussion

4.1. Asymmetric nucleation and forward growth of switched c-domains

The contribution of built-in fields to the nucleation and forward growth of the switched domains was verified through phase field modeling. To simulate *c*-domain switching, we considered a single domain PZT thin film with out-of-plane polarization sandwiched by Ni and $SrRuO_3$ electrodes (Fig. 8). A quasi-two-dimensional simulation cell with a size of $200 \times 1 \times 200$ voxels was chosen for the modeling. Two nuclei with 180° switched polarization were introduced at each electrode and a positive electrical bias of + 7.5 V was placed at the Ni electrode. The resulting domain switching process is shown in Fig. 8a. In the simulation the nucleus placed at the positively biased Ni electrode grows toward the SRO electrode while the nucleus at the negatively biased SRO electrode disappeared, in good agreement with experimental results. This can be explained by the electrical potential profile through the film shown in Fig. 8b and c. At the Ni electrode the local electric field was enhanced by the built-in field, which favored the growth of the nucleus on that side. This asymmetric nucleation and growth behavior was further demonstrated when the polarization orientation and the electric field were reversed (Fig. 9). In this case the nucleation and growth at the positively biased SRO electrode was favored. It is noted that the minimum electric potential bias required for the growth of nucleus is 0.5 V lower than the previous case. This difference is caused by the difference of the built-in potential (ΔV_{bi}) between the Ni electrode (0.65 V) and SRO electrode (0.9 V). These asymmetric behaviors can be interpreted as a direct consequence of the local enhancement of the electric field by the built-in field.

4.2. Asymmetric sideways growth of switched c-domains

As shown in Figs. 2b and 3b, the two electrodes in the MFM capacitor are distinguished by their interface structures, which influences the charge screening capability of the electrodes and thus the interaction with switched domains. It has been proposed that depolarization fields arise at the ferroelectric/electrode interface of an MFM capacitor when the polarization charge is not completely screened by the free electrons in the electrode [44]. For the atomically abrupt PZT/SRO interface, this is not the case because the free electrons in the SRO could compensate the polarization charge almost perfectly at the interface. When the SRO served as the counter-electrode, the growing domains readily established vertical charge-neutral orientations, which facilitated stable sideways growth along the interface [45] (Fig. 2a). This demonstrates that the compensation of the polarization charge, regardless of its sign, is accomplished almost perfectly by the free electrons in the SRO electrode, which prohibits the development of a significant dipole moment at the interface. Note that the conductive SRO is characterized by a relatively short screening length (~6 Å) [46], which is comparable with those of typical metal electrodes (<1 Å).

However, the contact between the Ni and PZT is different; it was interrupted by an interfacial layer with an average thickness of 1.5 nm (Fig. 3b). Moreover, the *a*-domains caused additional roughness at their intersections with the Ni/PZT interface, which increased the local thickness of the interfacial layer. This interfacial layer may have hindered the screening of the polarization charge at the Ni/PZT interface; that is, it increased the effective screening length of the Ni electrode (from 0.7 Å calculated for an ideal Ni electrode using the equation given by Mehta et al. [44] up to ~15 Å corresponding to the thickness of the interfacial layer). When this interface acted as the nucleation site during the negative switching, the negative polarization charge remained partially uncompensated within the charge depletion region of the Ni/PZT interface, which resulted in the development of a depolarization field and a decrease of the built-in potential (and the built-in field) [47,48]. The built-in potential recalculated for the Ni/PZT interface assuming the presence of a negative polarization charge ~1.5 nm from the Ni electrode (corresponding to the average thickness of the interfacial layer) was ~0.52 V. This is smaller than the built-in potential of 0.65 V introduced by the work function offset only (Fig. 1b). Furthermore, because the interfacial layer was not uniform in thickness, the forward growth of the switched domains was preferentially activated where the interfacial layer was the thinnest and thus the local effective field was the strongest. Note that only the domains A and B that were nucleated away from the *a*-domains grew quickly (Fig. 2a). When the Ni/PZT interface acted as the counter-electrode during the negative switching, the incomplete compensation of the positive polarization charge resulted in the development of a depolarization field. This tended to trap charges near the electrode, thereby suppressing the polarization switching and resulting in an increase in the coercive field [49]. During the positive switching, some domains near the Ni electrode appeared to persistently resist the switching up to an

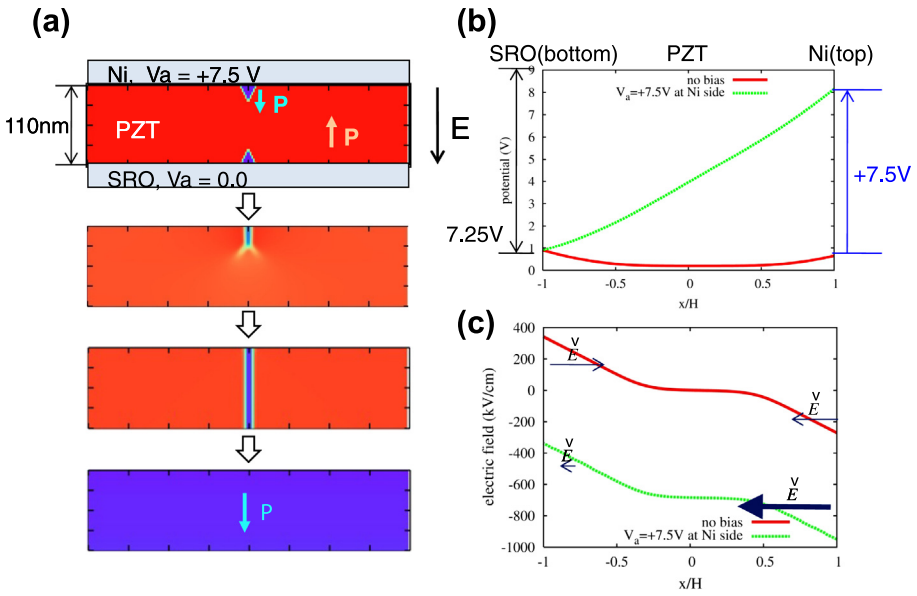

Fig. 8. Asymmetric nucleation and forward growth of a switched *c*-domain. (a) Phase-field simulation showing the domain nucleation and growth behavior under applied bias to the Ni electrode (+7.5 V). (b) Local electric potential distribution in the initial state under uniform external bias. (c) Local electric field distribution in the initial state under uniform external bias.

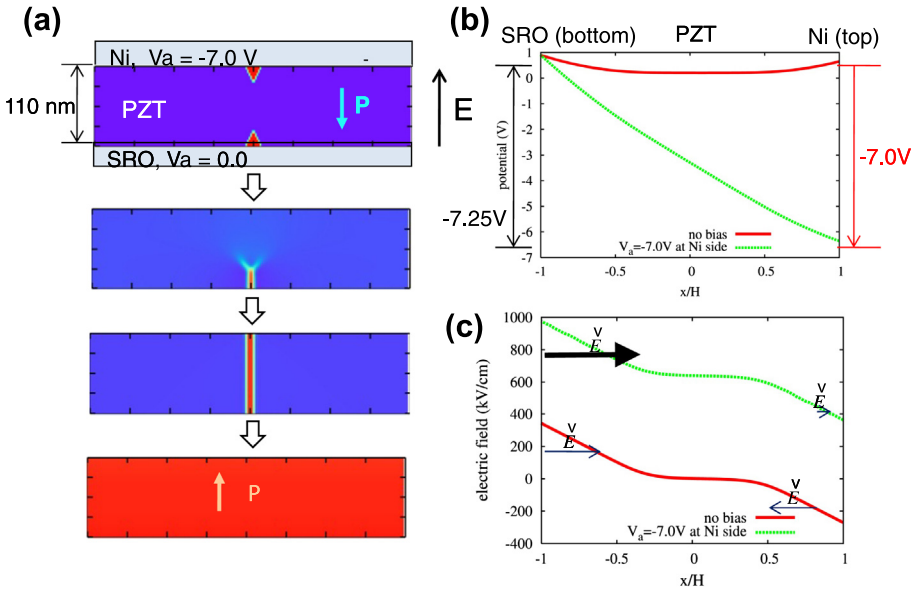

Fig. 9. Asymmetric nucleation and forward growth of a switched *c*-domain. (a) Phase-field simulation showing the domain nucleation and growth behavior under applied bias to the SRO electrode (−7.0 V). (b) Local electric potential distribution in the initial state under uniform external bias. (c) Local electric field distribution in the initial state under uniform external bias.

electric field of −1 MV cm^{-1}. It has been proposed that the depolarization fields are responsible for the persistent existence of unswitched domains at the ferroelectric/electrode interface [44]. In contrast, the negative switching to the $\mathbf{P}_{[00\bar{1}]}$ was readily completed at an electric field as low as 545 kV cm^{-1}, without leaving unswitched domains near the SRO electrode.

4.3. Switching of a-domains via 90° stripe domain formation

Phase field modeling was conducted in order to rationalize the proposed model on the evolution of 90° stripe domains described in Fig. 7. First, a simulation cell was constructed such that a switched *c*-domain encountered an *a*-domain during forward growth under an applied electric field (Fig. 10a). Upon reaching the *a*-domain, the switched *c*-domain quickly penetrated the *a*-domain and formed a sharp triangular shape that grew as a stripe along the boundary normal. The intergrowth of the *c*-domains into the *a*-domain can minimize the total bound charges created at the domain wall. The electrostatic potential map demonstrates that a large positive potential developed at the domain wall when the switched domain reached the *a*-domain due to the head-to-head polarization

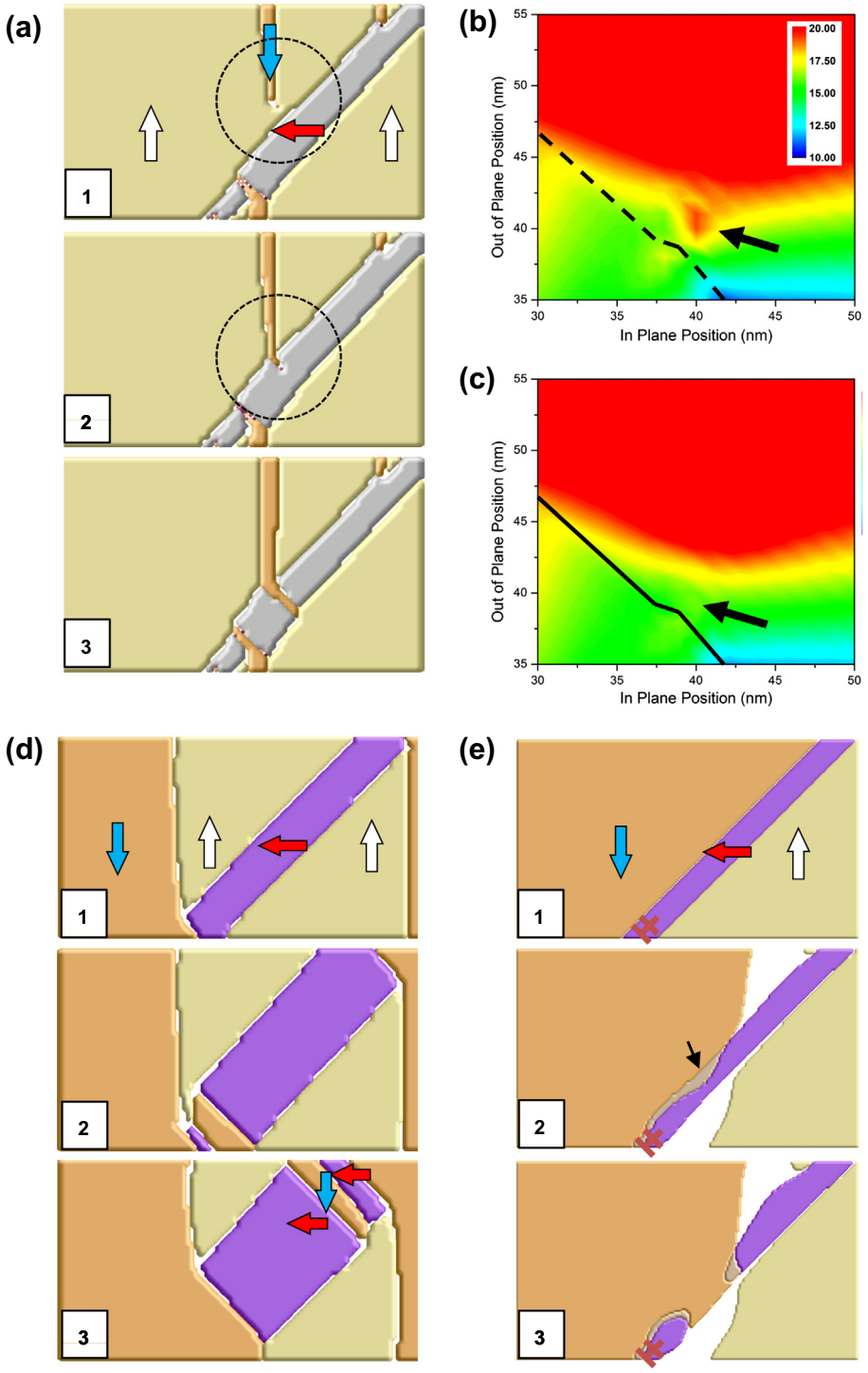

Fig. 10. Splitting of an *a*-domain into 90° stripe domains during 180° switching: phase field simulation. (a) Interaction of a *c*-domain with an *a*-domain related to the head-to-head polarization during forward growth. The switched *c*-domain grew quickly into the *a*-domain in a triangular shape. (b) Electrostatic potential map showing a large positive potential developing at the domain wall when the switched *c*-domain approached the *a*-domain due to the head-to-head polarization configuration (corresponding to the region marked with a circle in image 1). The potentials associated with the positive bound charges are indicated by black arrow. (c) Electrostatic potential map showing a smoother electrical potential profile when the triangular shaped domain was formed (the region marked with a circle in image 2). (d) Interaction between *c*-domains and an *a*-domain related to the head-to-head polarization in the course of sideways growth. The initial domain structure is shown in image 1. (e) Interaction between a *c*-domain and an *a*-domain pinned by misfit dislocations at the PZT/SRO interface. Note that the domain indicated by black arrow is a transient phase that has continuously varying polarization in the in-plane and out-of-plane polarization components, and the white areas do not have a polarization component sufficiently large to assign a specific domain type.

configuration (Fig. 10b). When the triangular-shaped *c*-domain formed within the *a*-domain, the electrostatic potential map exhibited a smoother electrical potential profile (Fig. 10c) as the positive bound charges were predominantly removed due to the head-to-tail polarization configuration obtained with the new triangular *c*-domain. In a separate phase field modeling, the initial domain structure was modified such that a switched *c*-domain met an *a*-domain during its sideways growth (Fig. 10d). As the switched *c*-domain moved toward the *a*-domain via the sideways growth, it grew into the *a*-domain preferentially from the top and bottom corners of the initial *a*-domain by forming 90° stripe domains. While the preferential switching of the top corner of the *a*-domain agreed well with the experiments (Figs. 6a and 7a and the schematic drawings in Fig. 7c), the bottom corner of the *a*-domain remained stable in the experiments with resisting undercutting by the switched *c*-domain. Fig. 10e shows the interaction between a *c*-domain and an *a*-domain which is pinned by misfit dislocations at the PZT/SRO interface. The obtuse corner side of the *a*-domain was initially switched to have a head-to-head polarization. In this case, the bottom corner of the *a*-domain remained stable while divots formed and continued growing through the *a*-domain to reduce the interfacial charge.

The intergrowth of the switched *c*-domain into the constrained volume of *a*-domain imposes a large elastic strain because the lattice mismatch associated with the reversal of the *a* and *c* lattice parameters must be accommodated at each (0 1 1) domain boundary of 90° stripe domains. Although this type of 90° ferroelastic switching appears unfavorable due to the large elastic and domain wall energy costs, the results suggest that it occurs when the decrease in electrostatic energy counterbalances the energy gain. In this case, the formation of the 90° stripe domain pattern decreased the depolarization field and the electrostatic energy by removing portions of the charged domain wall and rotating the net polarization orientation closer to the field direction [19,20]. With further increases in the electric field or switching time, the switched *c*-domains within the 90° stripe domains may grow gradually by consuming adjacent *a*-domains in a process similar to the two-step 90° switching that is frequently observed in bulk ferroelectric oxides [50]. Once the electric field is removed, part of stripe pattern is slowly erased, demonstrating that the 90° stripe domain structure is a metastable; it is only stable under a high electric field but relaxes when the field is removed. These observations suggest that the *a*-domains are active during the 180° switching of the out-of-plane polarization. This is the first time that the ferroelastic switching of the *a*-domains via 90° stripe patterning has been observed.

5. Conclusion

In situ TEM switching experiments were successfully implemented for a PZT capacitor and unambiguously confirmed the classical nucleation and growth model for the polarization switching of a ferroelectric thin film. In addition, a number of new and important findings are reported: (i) nucleation occurs preferentially at one ferroelectric/electrode interface determined primarily by the nature of the interface built-in fields; (ii) forward growth is controlled principally by the effective field distribution across the ferroelectric film, which follows the characteristics of a typical back-to-back Schottky diode; and (iii) sideways growth is limited by a depolarization field at the counter-electrode, which arises from the imperfect screening of the polarization charges. The present in situ TEM revealed that the ferroelastic *a*-domains are active during the 180° switching of the out-of-plane polarization and partly responsible for the asymmetry in the switching between the two polarization states. During the negative switching, the local depolarization fields induced across the *a*-domains tended to delay the sideways growth of the adjoining *c*-domains and simultaneously drove the intergrowth of the *c*-domains into the *a*-domain in order to reduce the depolarization field, which resulted in the formation of 90° stripe domains. This observation implies that some local switching events can occur during the overall switching process in order to compensate the depolarization fields, even at the expense of higher local energy. The proposed methods and findings contribute to the current understandings, will motivate additional detailed studies on the ferroelectric switching process, and will create a pathway to a more comprehensive understanding of the ferroelectric switching process for practical applications.

Acknowledgments

This study was supported mainly by the Basic Science Research Program through the National Research Foundation of Korea (NRF) funded by the Ministry of Education, Science and Technology (Grant 2010-0005834 and Grant 2011-0029406). The work at Penn State was supported by the US Department of Energy, Office of Basic Energy Sciences, Division of Materials Sciences and Engineering under Award DE-FG02-07ER46417. The work at ORNL was sponsored by the US Department of Energy, Basic Energy Sciences, Materials Science and Engineering Division.

Appendix A. Supplementary material

Supplementary data associated with this article can be found, in the online version, at http://dx.doi.org/10.1016/j.actamat.2013.07.051.

References

[1] Scott JF. Science 2007;315:954.
[2] Catalan G, Seidel J, Ramesh R, Scott JF. Rev Mod Phys 2012;84:119.
[3] Balke N, Gajek M, Tagantsev AK, Martin LW, Chu YH, Ramesh R, et al. Adv Funct Mater 2010;20:3466.
[4] Kim TH, Baek SH, Yang SM, Kim YS, Jeon BC, Lee D, et al. Appl Phys Lett 2011:99.

[5] Tagantsev AK, Pawlaczyk C, Brooks K, Setter N. Integrated Ferroelectrics 1994;4:1.
[6] Prosandeev S, Bellaiche L. Phys Rev B 2007:75.
[7] Landauer R. J Appl Phys 1957;28:227.
[8] Bratkovsky AM, Levanyuk AP. Phys Rev Lett 2000;84:3177.
[9] Maksymovych P, Balke N, Jesse S, Huijben M, Ramesh R, Baddorf AP, et al. J Mater Sci 2009;44:5095.
[10] Huey BD, Premnath RN, Lee S, Polomoff NA. J Am Ceram Soc 2012;95:1147.
[11] Chu MW, Szafraniak I, Scholz R, Harnagea C, Hesse D, Alexe M, et al. Nat Mater 2004;3:87.
[12] Su D, Meng QP, Vaz CAF, Han MG, Segal Y, Walker FJ, et al. Appl Phys Lett 2011:99.
[13] Ganpule CS, Nagarajan V, Li H, Ogale AS, Steinhauer DE, Aggarwal S, et al. Appl Phys Lett 2000;77:292.
[14] Jesse S, Rodriguez BJ, Choudhury S, Baddorf AP, Vrejoiu I, Hesse D, et al. Nat Mater 2008;7:209.
[15] Speck JS, Pompe W. J Appl Phys 1994;76:466.
[16] Lee HN, Nakhmanson SM, Chisholm MF, Christen HM, Rabe KM, Vanderbilt D. Phys Rev Lett 2007:98.
[17] Nelson CT, Gao P, Jokisaari JR, Heikes C, Adamo C, Melville A, et al. Science 2011;334:968.
[18] Gao P, Nelson CT, Jokisaari JR, Baek SH, Bark CW, Zhang Y, et al. Nature Commun 2011:2.
[19] Roelofs A, Pertsev NA, Waser R, Schlaphof F, Eng LM, Ganpule C, et al. Appl Phys Lett 2002;80:1424.
[20] Ganpule CS, Nagarajan V, Hill BK, Roytburd AL, Williams ED, Ramesh R, et al. J Appl Phys 2002;91:1477.
[21] Gao P, Nelson CT, Jokisaari JR, Zhang Y, Baek SH, Bark CW, et al. Adv Mater 2012;24:1106.
[22] Chang HJ, Kalinin SV, Yang S, Yu P, Bhattacharya S, Wu PP, et al. J Appl Phys 2011:110.
[23] Chen L, Ouyang J, Ganpule CS, Nagarajan V, Ramesh R, Roytburd AL. Appl Phys Lett 2004;84:254.
[24] Lu H, Bark CW, de los Ojos DE, Alcala J, Eom CB, Catalan G, et al. Science 2012;336:59.
[25] Tanaka M, Honjo G. J Phys Soc Jpn 1964;19:954.
[26] Fujimoto F. J Phys Soc Jpn 1959;14:1558.
[27] Hu HL, Chen LQ. Mater Sci Eng A-Struct Mater Prop Microstruct Process 1997;238:182.
[28] Li YL, Hu SY, Liu ZK, Chen LQ. Appl Phys Lett 2001;78:3878.
[29] Li YL, Hu SY, Liu ZK, Chen LQ. Acta Mater 2002;50:395.
[30] Li YL, Chen LQ, Asayama G, Schlom DG, Zurbuchen MA, Streiffer SK. J Appl Phys 2004;95:6332.
[31] Haun MJ, Ph.D. thesis, Pensylvania State University; 1988.
[32] Haun MJ, Furman E, Jang SJ, Cross LE. Ferroelectrics 1989;99:13.
[33] Haun MJ, Furman E, Jang SJ, Mckinstry HA, Cross LE. J Appl Phys 1987;62:3331.
[34] Haun MJ, Furman E, Mckinstry HA, Cross LE. Ferroelectrics 1989;99:27.
[35] Haun MJ, Zhuang ZQ, Furman E, Jang SJ, Cross LE. Ferroelectrics 1989;99:45.
[36] Li YL, Hu SY, Chen LQ. J Appl Phys 2005:97.
[37] Sze SM, Coleman DJ, Loya A. Solid-State Electronics 1971;14:1209.
[38] Sudhama C, Campbell AC, Maniar PD, Jones RE, Moazzami R, Mogab CJ, et al. J Appl Phys 1994;75:1014.
[39] Merz WJ. Phys Rev 1954;95:690.
[40] Gureev MY, Tagantsev AK, Setter N. Phys Rev B 2011:83.
[41] Misirlioglu IB, Alpay SP, Aindow M, Nagarajan V. Appl Phys Lett 2006:88.
[42] Chu MW, Szafraniak I, Hesse D, Alexe M, Gosele U. Phys Rev B 2005:72.
[43] Catalan G, Lubk A, Vlooswijk AHG, Snoeck E, Magen C, Janssens A, et al. Nat Mater 2011;10:963.
[44] Mehta RR, Jacobs JT. J Appl Phys 1973;44:3379.
[45] Mokry P, Tagantsev AK, Fousek J. Phys Rev B 2007:75.
[46] Junquera J, Ghosez P. Nature 2003;422:506.
[47] Pintilie L, Alexe M. J Appl Phys 2005:98.
[48] Pintilie L, Vrejoiu I, Rhun GL, Alexe M. J Appl Phys 2007:101.
[49] Tagantsev AK, Gerra G. J Appl Phys 2006:100.
[50] Jiang B, Bai Y, Chu WY, Su YJ, Qiao LJ. Appl Phys Lett 2008:93.